Cement and Concrete Composites 124 (2021) 104255

Contents lists available at ScienceDirect

Cement and Concrete Composites

journal homepage: www.elsevier.com/locate/cemconcomp

Research Paper

Mechanical behavior of carbonated MgO-based Engineered Cementitious Composite (ECC) after high temperatures exposure

Haoliang Wu [a,b], Duo Zhang [a,1], Brian R. Ellis [a], Victor C. Li [a,*]

[a] Department of Civil and Environmental Engineering, University of Michigan, Ann Arbor, MI, 48109, USA
[b] Department of Civil and Environmental Engineering, Hong Kong University of Science and Technology, Clear Water Bay, Kowloon, Hong Kong SAR, China

ARTICLE INFO

Keywords:
Carbonated MgO
Engineered cementitious composite
Mechanical behavior
Interface parameters
Micromechanical analysis

ABSTRACT

Carbonated MgO-based Engineered Cementitious Composite (ECC) has ultrahigh tensile ductility and tight crack width control behavior. However, the expectation of improved fire-resistant has not been confirmed. This study explored the alterations to mechanical and microstructure characteristics of this material after exposure to temperatures up to 500 °C. Material mass loss, compressive strength, tensile strength, strain capacity, and matrix fracture toughness were measured. Scanning electron microscopy, mercury intrusion porosimetry, thermogravimetric analysis, and X-ray diffraction were used to probe the degradation of the cement matrix and fibers. The effect of elevated temperature on carbonated MgO-based ECC was further assessed via examination of the micromechanical behavior of the fiber-matrix. The objective of this research was to assess the performance of carbonated MgO-based ECC exposed to fire hazards. The tensile ductility of carbonated MgO-based ECC was found to be enhanced when exposed to ~100 °C as compared with those at room temperature ~20 °C. Further increase in exposure temperature, however, posed a negative impact on the composite compressive strength, ultimate tensile strength, and ability to control crack width. The results provide a useful database for further investigations into carbonated MgO-based ECC for fire safety enhancement.

1. Introduction

Engineered cementitious composites (ECC, also known as strain-hardening cementitious composites (SHCC)) [1,2], feature an ultra-high tensile ductility over 2% and intrinsically tight micro-crack width below 100 μm [2–8]. However, the higher content of ordinary Portland cement (OPC) in ECC leads to an undesirable higher carbon intensity when compared with regular concrete. In the past decades, attempts have been made to address this concern by substituting OPC with supplementary cementitious materials (e.g., fly ash, silica fume (SF), granulated blast furnace slag (GGBS), metakaolin (MK), and rice husk ash (RHA)) to improve ECC's workability, durability and environmental footprint [9–12]. Among emerging alternative binders, reactive MgO cement is attractive due to its lower production temperatures than OPC [7,10,13–15]. Further, this binder gains strength by reacting with CO_2 to form carbonated reactive magnesia cement systems (RMC) [14,16–18]. Previous studies reported that the RMC systems sequester substantial amounts of CO_2 through carbonation reactions, which could further reduce CO_2 emissions by forming a variety of hydrated magnesium carbonates (HMCs) [16,17]. The HMCs mainly include nesquehonite ($MgCO_3{\cdot}H_2O$), hydromagnesite ($Mg_5(CO_3)_4(OH)_2{\cdot}4H_2O$), and dypingite ($Mg_5(CO_3)_4(OH)_2{\cdot}5H_2O$) [13]. The formation of these carbonate phases can reduce the porosity by expansion and then provide strength via the formation of a continuous network [19,20].

Recently, carbonated MgO-based binder has been introduced to ECC (MgO-based ECC) [5,10]. The carbonated MgO-based ECC attained excellent tensile performance, with strain capacity and ultimate strength reaching 4.0% and 4.1 MPa, respectively, over 1 day accelerated carbonation process [5,10]. The application of MgO-based ECC could reduce the embodied CO_2 emission and raw materials cost by ~65% and ~60%, respectively [10]. Further, the self-healing properties of carbonated MgO-based ECC have been investigated to provide insight for lifecycle analysis of energy consumption [5]. It was reported that the robust self-healing capability could be attributed to the tight micro-cracks width (less than 60 μm) and formation of nesquehonite hydromagnesite crystallites [5,21].

The carbonated MgO-based ECC is a relatively new and green material with benefits as mentioned above. Understanding its behavior

* Corresponding author.
E-mail address: vcli@umich.edu (V.C. Li).
[1] Contribution equal to the first author.

https://doi.org/10.1016/j.cemconcomp.2021.104255
Received 8 February 2021; Received in revised form 2 July 2021; Accepted 9 September 2021
Available online 14 September 2021

Table 1
Mix proportion of carbonated MgO-based ECC (with respect to binder[a] ratio).

ID	MgO	Fly ash	Water	SHMP[b]	SP	PVA Fiber[c]
MgO-based ECC	1	1	1.04	0.104	0.015	2.0

[a] Binder refers to MgO and fly ash.
[b] Sodium hexametaphosphate (SHMP) was 10% by water mass.
[c] PVA fiber content, by volume %.

under aggressive environmental conditions will improve confidence in its utilization. Although several investigations have reported on this composite group [5,10,22,23] in the term of robust ductility, tight crack width, and self-healing capability, the behavior of carbonated MgO-based ECC subjected to elevated temperatures, such as under fire exposure, has been scarcely studied.

The mechanical behavior of OPC-based ECC materials is known to be sensitive to elevated temperatures [24,25]. For abnormal and severe fire hazard conditions, the temperature of building structures can reach 100–800 °C as specified in ISO 19706 [26]. The compressive strength of OPC-based ECC dropped by about 50% after exposure to 600 °C, and the tensile strength and strain capacity were reduced by up to 40% when the temperature increased from 100 to 600 °C [25]. Interestingly, no spalling was observed in the OPC-based ECC, although increased micro-pores and nano-cracks were reported at temperatures above 200 °C [25,27]. Given that the HMCs and fibers in MgO-based ECC are essential for ensuring higher tensile ductility and tight crack widths, it is of interest to determine the ability of MgO-based ECC in maintaining these tensile properties under elevated temperatures.

The stability of carbonated MgO-based binder has attracted researchers' attention in fire-resistance performance. Theoretically, elevated temperature would lead to a transformation of HMCs in the carbonated MgO-based binder [19]. The literature on high temperature effects on carbonated MgO-based binder focus on the change in compressive strength and transformation of microstructures, and decomposition of various HMCs (i.e., including the dehydration, dehydroxylation, and decarbonisation steps) when exposed to different ambient conditions [19,28–30]. It was shown that the carbonated MgO-based materials resulted in a 12% decline in compressive strength at 80 °C and a 61% drop at 550 °C [30]. Such compressive strength drop was due to the transformation of carbonates into less hydrated phases and CO_2 gas [31]. The cracks and larger voids created by the degradation and decomposition of carbonated MgO-based binder also reduce material strength [32,33]. The transformation of HMCs started at ~52 °C by decomposing nesquehonite and then at around ~255 °C by decomposing hydromagnesite [34,35]. Although the influence of high temperature on the mechanical performance of carbonated MgO-based binder has been thoroughly investigated, none of these studies were performed on carbonated MgO-based ECC. As fiber reinforcement has been reported to mitigate the loss of compressive strength in OPC-based ECC [36–41], its beneficial effect on carbonated MgO-based ECC under high temperature is of interest and should be verified.

The present research investigates the effects of elevated temperatures on the alteration of mechanical and microstructural characteristics of carbonated MgO-based ECC. The composite mass loss, compressive strength, tensile strength and ductility, and fiber, matrix, and fiber/matrix interface characteristics at 20 °C, 50 °C, 100 °C, 200 °C, and 500 °C, were studied. Additionally, the crack patterns and fracture surfaces of specimens were investigated by high-resolution optical microscopy and scanning electron microscopy (SEM). Finally, the carbonated MgO matrix microstructure and hydration products after exposure to elevated temperatures were determined by mercury intrusion porosimetry (MIP), and thermogravimetric analysis (TGA), and X-ray diffraction (XRD), respectively. This research fills the knowledge gap regarding the thermal-mechanical behavior of carbonated MgO-based ECC under elevated temperatures. Such data on carbonated MgO-based ECC should shed light on its potential for application in fire-resistant building structures.

2. Materials and methodology

2.1. Materials

A MgO-based ECC with MgO/fly ash ratio of 1.0 and water to binder (MgO + fly ash) ratio of 0.52 by mass was used in this study. The mix proportion is given in Table 1. Light-burnt MgO conforming to ASTM C151 [42] requirements, Class-F fly ash per ASTM C618 [43], tap water, sodium hexametaphosphate (SHMP, $Na(PO_3)_6$), and superplasticizer (SP) were used. The light-burnt MgO (MAGOX® premium grade) passed the standard #325 mesh with 99.5% and #100 mesh with 100%. The fly ash was supplied by Headwaters Resources Inc (from Michigan, USA). The oxide compositions of the MgO and fly ash are listed in Table 2. As SHMP could significantly reduce free water consumption and enhance the dispersion capacity of the SP [44], SHMP (from Alfa Aesar™) and SP (from W.R. Grace & Co.) were utilized in combination to achieve sufficient workability for the fresh mixture. The 8 mm long PVA fibers (from Kuraray Ltd., Japan) with maximum elongation of 6%, Young's modulus of 42.8 GPa, density of 1300 kg/m^3, and coated with 1.2% oil were used in this study.

2.2. Sample preparation

The MgO-based ECC mixtures were mixed in a 4-L capacity mixer. The dry ingredients, including reactive MgO and fly ash, were first mixed for 2 min at a speed of 100 r/min. The pre-mixed SHMP-SP solution was then added to the dry ingredients and was further mixed for 3 min at a speed of 150 r/min to produce a uniform paste. Finally, the PVA fibers were added slowly into the mixture which was mixed for an additional 5 min until reaching a good fluidity. The fresh MgO-based ECC mixtures were cast into cubic and dogbone-shaped molds (Fig. 1), as described in Wu et al. [10]. These molds were sealed with a plastic bag and set in air for 21 h before demolding the specimens which were

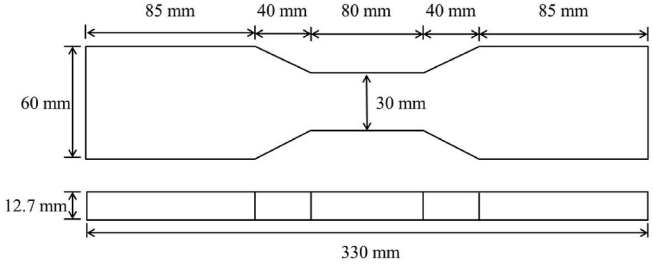

Fig. 1. Dimensions of dogbone-shaped specimen for uniaxial tension test.

Table 2
Oxide compositions of MgO and class-F fly ash.

Oxides[a]	SiO_2	Al_2O_3	SO_3	MgO	P_2O_5	K_2O	TiO_2	Fe_2O_3	CaO	Cl	LOI[b]
MgO (%)	0.31	0.20	–	95.76	–	–	0.01	0.13	0.81	0.03	2.75
Fly ash (%)	52.19	22.23	2.16	0.93	0.11	2.56	1.01	13.49	3.40	0.01	1.01

[a] Oxides are analyzed by X-ray fluorescence spectrometry.
[b] Loss on ignition at 950 °C.

Fig. 2. Visible degradation process of PVA fiber at various temperatures.

then cured in CO_2. The curing condition was set as $T = 20 \pm 2$ °C and relative humidity (RH) = 65 ± 5%. The carbonation chamber was continuously supplied with 99.8% purity CO_2 gas at 2.0 bars pressure to conduct the carbonation process. The MgO-based ECC specimens were carbonated for 1 day.

2.3. Methodology

2.3.1. Elevated temperature exposure

Once carbonation curing was completed, the MgO-based ECC specimens were heated in a muffle furnace (Vulcan 3–550). The target exposure temperatures were 50 °C, 100 °C, 200 °C, and 500 °C. Specimens kept at 20 °C were used as controls. The heating rate was approximately 5 °C/min to simulate a large-scale fire hazard [45]. The specimens were held in the furnace for 1 h after reaching the target temperature [46]. They were then removed from the furnace and air-cooled to room temperature for mechanical tests. Additionally, fiber-free mortar and PVA fiber were subjected to the same heating protocol for comparison and to directly observe the effects of elevated temperature on fiber behavior.

2.3.2. Compression and uniaxial tension

After the heat treatment, compressive strength was obtained from the 50-mm cube specimens at a loading rate of 0.54 ± 0.18 MPa/s per ASTM C109/C109 M [47]. Dogbone-shaped specimens were used for uniaxial tension per Japan Society of Civil Engineers (JSCE [48]). An Instron® instrument with a loading capacity of 10 kN and a 0.5 mm/min loading rate was used for tension. After testing, the residual crack numbers and widths in the 80-mm gauge region of the dogbone-shaped specimen were measured along the center line using an optical microscope (infinity X–C21, with 10 μm resolution). The crack widths were measured after the load was released, thus the total residual crack widths would be less than the ultimate tensile deformation, due to a partial crack closure during unloading. The fracture surfaces of the specimens were examined using scanning electron microscopy (JEOL IT500).

2.3.3. Matrix fracture toughness and single fiber pull out test

Based on micromechanics, two basic design criteria [2] should be satisfied for strain-hardening in ECC: 1) the first cracking strength σ_{fc} must not exceed the fiber bridging capacity σ_0 across the crack (Eq. (1)); 2) the crack tip toughness J_{tip} must be less than the complementary energy J_b' (Eq. (2)).

$$\sigma_0 > \sigma_{fc} \tag{1}$$

$$J_b' \equiv \sigma_0\delta_0 - \int_0^{\delta_0} \sigma(\delta)d\delta > J_{tip} \cong K_m^2 \Big/ E_m \tag{2}$$

where σ(δ) is the fiber bridging stress versus crack opening relationship, σ_0 is the maximum bridging stress corresponding to the crack opening δ_0. The delicate balance of the micromechanical parameters associated with the fiber, matrix, and fiber/matrix interface is necessary to obtain robust tensile ductility.

To understand the impact of elevated temperature on ECC's micromechanical parameters, specimens for matrix fracture toughness and single fiber pull-out tests were prepared. The specimens were then subjected to the same heating protocol as that for ECC.

The single fiber pull-out test was conducted to reveal the impact of the elevated temperature on the fiber/matrix interfacial properties, including the interfacial frictional bond τ_0 and chemical bond G_d. A load cell with 44.48 N capacity was used, and the loading rate was kept at 0.01 mm/s. The complementary energy J_b' and fiber bridging capacity σ_0 were deduced from the $\sigma(\delta)$ relation governed by fiber and fiber/matrix interfacial properties.

The matrix fracture toughness K_m was determined using three-point bending specimens without fiber, as per ASTM E 399 [49]. The specimen was notched at the bottom center section of the beam with a notch depth and beam height ratio of 0.5. K_m was computed using Eqs. 3 and 4 together with the measured peak load P_b (N). E_m is the matrix Young's modulus, which is calculated by the empirical formula (CEB-FIP Model Code 1990 [50]) as shown in Eq. (5).

$$K_m = \frac{P_b \times S}{bh^{1.5}} \times f(a_0/h) \tag{3}$$

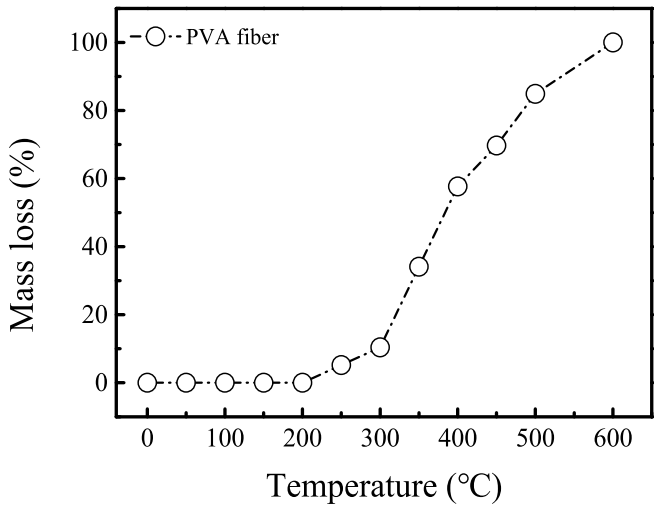

Fig. 3. Quantification of the decomposition process of PVA fiber with thermogravimetric analysis.

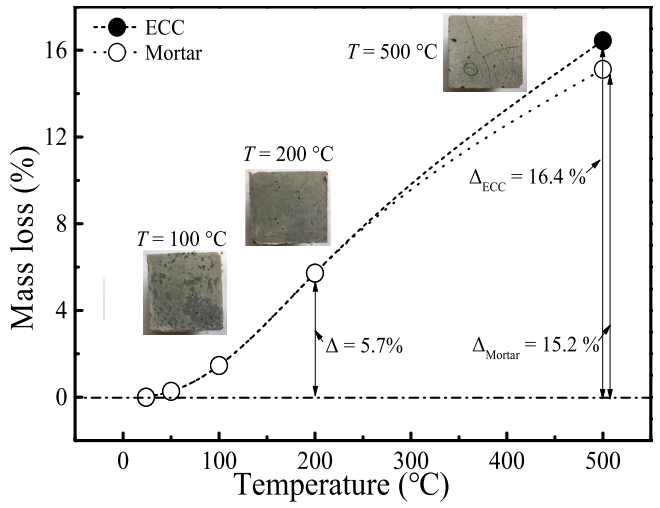

Fig. 4. The effects of temperature exposure on mass loss of carbonated MgO-based mortar and ECC.

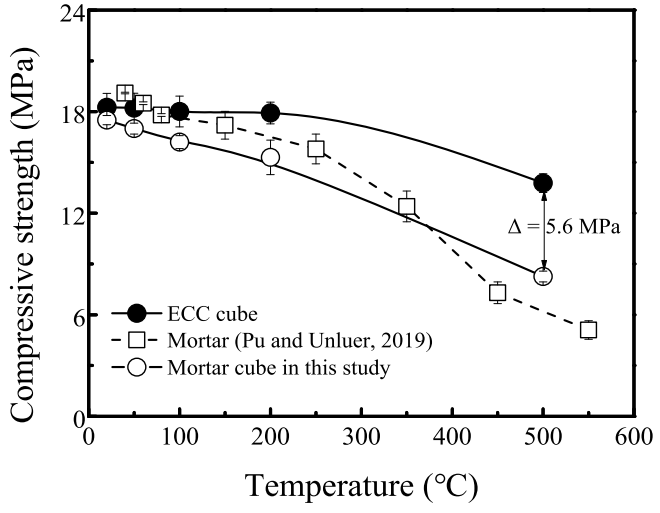

Fig. 5. Temperature exposure effect on compressive strength of carbonated MgO-based ECC and mortars.

$$f\left(\frac{a_0}{h}\right)=\frac{3\times(a_0/h)^{0.5}\times\left\{1.99-\left(\frac{a_0}{h}\right)\times\left(1-\frac{a_0}{h}\right)\times\left[2.15-\frac{3.93a_0}{h}+2.7\left(\frac{a_0}{h}\right)^2\right]\right\}}{2\times(1+2a_0/h)\times(1-a_0/h)^{1.5}} \quad (4)$$

$$E_m=0.85\times2.15\times10^4\times(f_c/10)^{1/3} \quad (5)$$

where S is the span (100 mm) of the beam specimen, a_0 is the notch depth (20 mm), b and h are the width and height of the beam (mm), and f_c is the matrix compressive strength (MPa).

2.3.4. MIP, TGA/DTA, and XRD analyses

After the high temperature treatment, the cooled MgO-based ECC specimens were used for MIP tests to analyze the pore size distribution. Approximately 1 cm^3 of carbonated material was collected from the dogbone-shaped specimen to conduct the MIP analysis using an AutoPore IV 9510. The collected samples were further crushed into powder and sieved through a 63 μm sieve to remove fiber for TGA and XRD tests. A Model Q500 TGA with helium and an X-ray diffractometer from Rigaku SmartLab with CuKα radiation were using to detect TGA and XRD data, respectively. The TGA test temperatures ranged from 30 to 1000 °C at a heating rate of 5 °C/min. The XRD diffraction pattern was collected in the range of 5°–55° (2θ) with a scanning speed of 0.02°/step.

3. Results and discussion

3.1. Mass loss and appearance of specimens

Fig. 2 shows the visual degradation of PVA fiber from 20 °C to 500 °C. The PVA fiber was lightly burnt as the temperature reached 200 °C and became dark as the temperature exceeded 250 °C. The PVA fiber was carbonized beyond 300 °C and completely decomposed at 500 °C. The thermogravimetric data (Fig. 3) indicate that the PVA fiber was slightly decomposed during 200 °C – 250 °C, and sharply decomposed after 300 °C.

The mass losses of carbonated MgO-based ECC and mortar cubes were studied. The specimens were weighed before and after heating and the mass loss was recorded (Fig. 4). The mass loss of ECC at 200 °C and 500 °C was 5.7% and 16.4%, respectively. The mass loss of the mortar was similar to that of the ECC specimens at temperatures below 200 °C, but was less (by ~1.2%) at an exposure temperature of 500 °C. Within this temperature range, mass loss is attributed to water evaporation, hydrated magnesium carbonates decomposition [29,34], and fiber melting. Surface cracks were observed on the specimens when the temperature exceeded 200 °C, which might be attributed to the increased internal pressure created by the capillary pore water vapor under elevated temperatures [32,33,41]. Cracks on specimens exposed to 500 °C were significantly larger due to the melting of PVA fiber beyond 230 °C [37], creating a network of interconnected channels.

3.2. Elevated temperatures effect on compressive properties

The effect of elevated temperatures on the compressive strength of ECC cubes is shown in Fig. 5. The compressive strength results of each sample were compared with the control mortars. For the mortars, the compressive strength gradually decreased from 17.8 MP a to 8.2 MPa as the temperature increased from 20 °C to 500 °C. The same trend was observed in prior research [28] on reactive-MgO mortar specimens cured under accelerated carbonation (CO_2 concentration = 10%, $T = 30 \pm 2$ °C and RH = 80 ± 5%). The decline in compressive strength was attributed to the decomposition of the hydrated magnesium carbonates (i.e., nesquehonite, hydromagnesite, and dypingite). For instance, previous studies reported the decomposition of nesquehonite into more stable carbonates at temperatures higher than 52 °C [35], and the

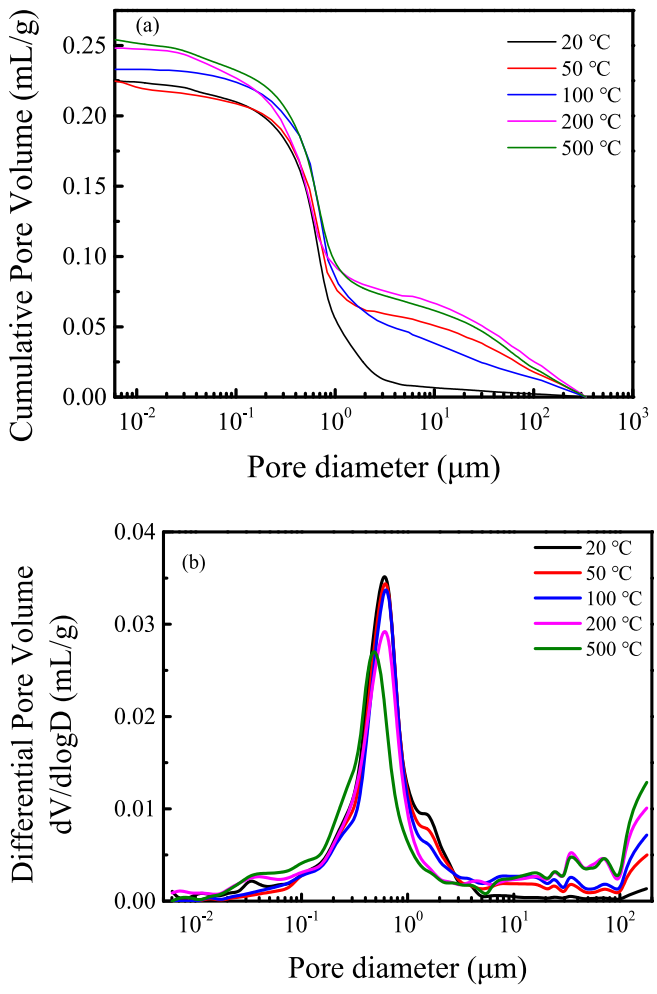

Fig. 6. Cumulative intruded volume and differential distribution curve the carbonated MgO-based ECC.

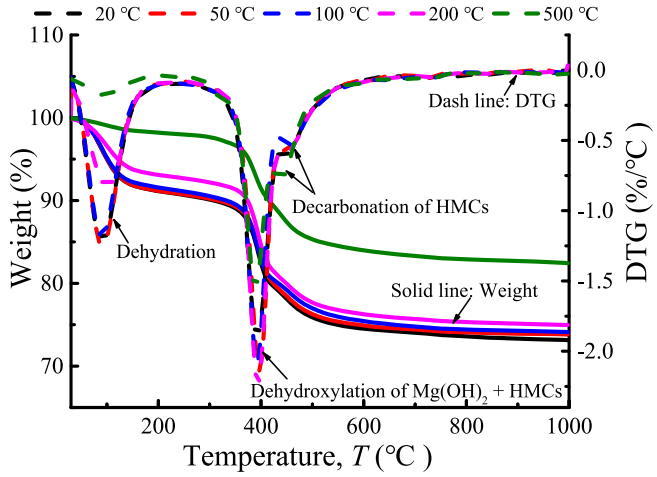

Fig. 7. Thermogravimetric analysis of MgO-based ECC (without fiber) under various exposure temperatures.

hydromagnesite gradually decomposed as the temperature increased to around 255 °C [29,34]. Additionally, the bound water loss would produce high vapor pressure within the pore at these high-temperature regimes, resulting in the formation of micro-cracks in the mortar [51].

For the ECC specimens, the compressive strength slightly decreased

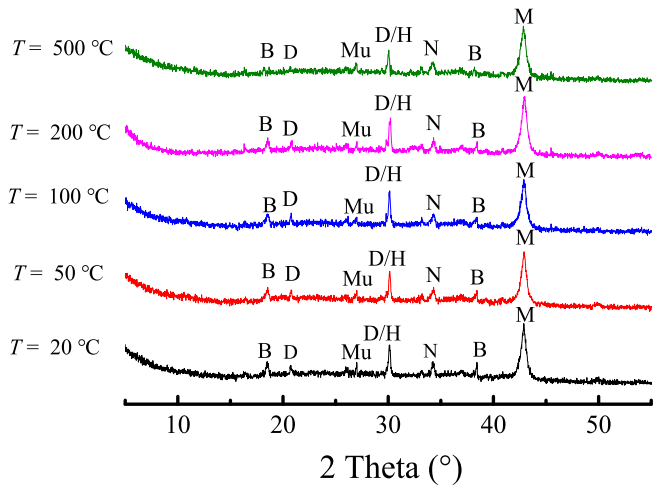

Fig. 8. X-ray diffractograms of carbonated MgO-based ECC (without fiber) under various exposure temperatures (B: brucite; D: dypingite, N: nesquehonite, Mu: mullite, H: hydromagnesite; M: MgO).

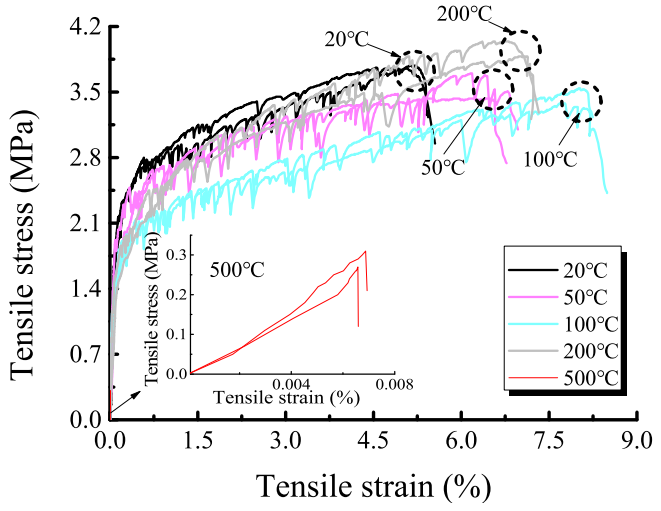

Fig. 9. Uniaxial tensile stress-strain curves for carbonated MgO-based ECC at various temperatures exposure.

Table 3
Tensile properties of carbonated MgO-based ECC.

Temperature	20 °C	50 °C	100 °C	200 °C	500 °C
First cracking strength (MPa)	2.01 ± 0.11	2.03 ± 0.02	2.11 ± 0.04	1.95 ± 0.12	0.28 ± 0.05
Tensile strain capacity (%)	5.13 ± 0.48	6.30 ± 0.32	7.91 ± 0.33	6.89 ± 0.56	0.007 ± 0.001
Ultimate tensile strength (MPa)	3.68 ± 0.22	3.54 ± 0.12	3.55 ± 0.16	3.96 ± 0.13	0.29 ± 0.12

from 18.3 MPa to 17.9 MPa as temperature increased from 20 °C to 200 °C. Compared to mortars, the reduction in compressive strength loss (1.9% for ECC vs. 12.6% for mortars) can be attributed to the reduced micro-cracking damage in ECC due to fiber bridging. The compressive strength of ECC dropped by 24.5% to 13.8 MPa as temperature increased to 500 °C, indicating damage caused by the decomposition of carbonate phases and PVA fibers. The retained strength is 5.6 MPa above that of the mortar control.

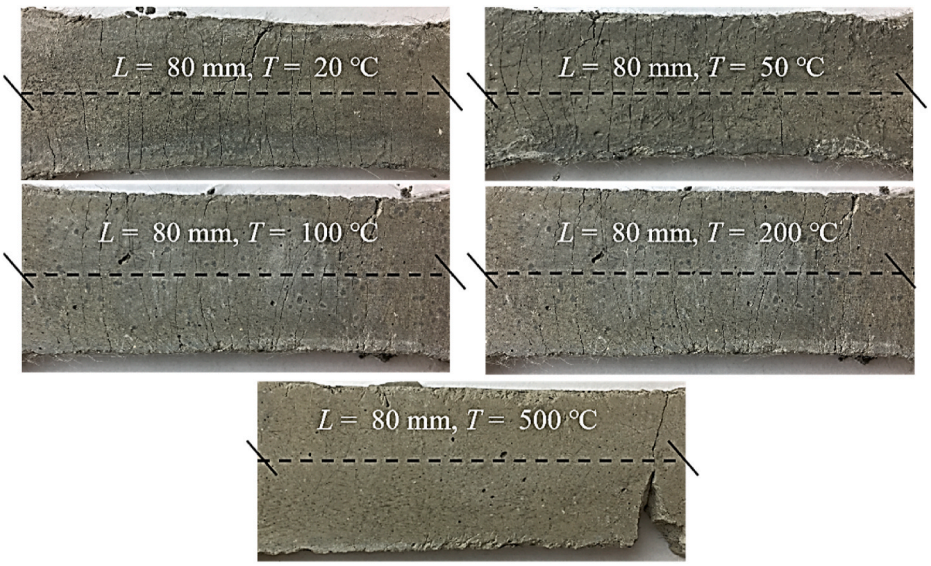

Fig. 10. Typical crack pattern of carbonated MgO-based ECC after various exposure temperatures
(a) T = 20 °C
(b) T = 100 °C
(c) T = 200 °C (d) T = 500 °C.

Table 4
Summary of residual crack patterns from tensile specimens.

Temperature	Crack numbers	Total residual crack width (μm)	Avg. Crack width (SD) (μm)
20 °C	47 ± 3	1571 ± 131	33.45 (±17.32)
50 °C	55 ± 2	2272 ± 101	41.31 (±20.18)
100 °C	68 ± 6	3234 ± 248	47.56 (±19.34)
200 °C	59 ± 4	2943 ± 133	49.89 (±19.27)
500 °C	N[a]	N[a]	N[a]

N[a]: Not applicable to specimens exposed to 500 °C.
SD: standard deviation.

3.3. Microstructure analysis

3.3.1. Mercury intrusion porosimetry

The cumulative and differential pore volume curves for the carbonated MgO-based ECC exposed to temperatures from 20 °C to 500 °C are presented in Fig. 6 (a) and **(b)**. The presented curves are used to evaluate the total porosity and pore size distribution.

The cumulative pore volume increased with increasing temperature from 20 °C to 500 °C. Two stages of the pore volume increase can be observed in Fig. 6 (a), including a slight increase during 20 °C–50 °C and a significant increase from 100 °C to 500 °C. This is attributed to bound water evaporation as the temperature rose from 20 °C to 50 °C [51], and the decomposition of carbonate phases (nesquehonite, hydromagnesite, and dypingite) and PVA fibers as the temperature rose from 100 °C to 500 °C. The total pore volume was 0.225 ml/g, 0.236 ml/g, and 0.258 ml/g for 20 °C, 100 °C and 500 °C, respectively.

Fig. 6 (b) presents the differential pore size distribution curves in which critical pore diameter corresponds to the peak of the differential curve. The peak was found to be between 0.6 μm and 180 μm pore diameters. The differential curves indicated that the pore size was dominated by large capillary pores (0.05–10 μm) and air voids (>10 μm) in carbonated MgO-based ECC. As compared to specimens at 20 °C, the increased temperature led to the peak at around ~0.6 μm shifting towards smaller pore sizes (0.01–0.05 μm), owing to the decomposition of HMCs and bound water evaporation. The increased pore size is a plausible cause of the decrease of compressive strength with temperatures as shown in Fig. 5.

3.3.2. Thermogravimetric analysis

The TGA results of carbonated MgO-based ECC (without fiber) are presented in Fig. 7. There are two major and one small decomposition steps in the presented data. The release of bound water from hydrated magnesium carbonates and water evaporation was observed between 50 °C and 120 °C, with strong endothermic peaks corresponding to the decomposition reaction as revealed in Eqs. (6) - (7). The decomposition of nesquehonite and brucite is responsible for the second strong endothermic peaks at ~380 °C. The dehydroxylation of hydromagnesite leads to a smaller peak at around ~440 °C. In turn, the lower amount of nesquehonite, brucite, but greater amount of dehydroxylation of hydromagnesite resulted in a lower peak intensity at ~380 °C but a higher peak intensity at ~440 °C as the temperature increased to 500 °C [35]. The reaction for the decomposition of nesquehonite [52], brucite and dehydroxylation of hydromagnesite are presented in Eqs. (8)–(10). The decomposition of HMCs and the appearance of microcracks (**Eq. (7)**) during the heating process results in a larger pore volume (Fig. 6) and slightly lower compressive strength (Fig. 5).

$$4MgCO_3\%Mg(OH)_2\%4H_2O \rightarrow 4MgCO_3\%Mg(OH)_2 + 4H_2O \quad (6)$$

$$H_2O\ (Liquid) \rightarrow H_2O\ (gas) \quad (7)$$

$$5(MgCO_3\%3H_2O) \rightarrow Mg_5(CO_3)_4(OH)_2\%XH_2O + CO_2 + (14-x)H_2O \quad (8)$$

$$Mg(OH)_2 \rightarrow MgO + H_2O \quad (9)$$

$$Mg_5(CO_3)_4(OH)_2\%xH_2O \rightarrow 5MgO + 4CO_2 + (x+1)H_2O \quad (10)$$

3.3.3. X-ray diffraction

Fig. 8 shows the XRD patterns of carbonated MgO-based ECC (without fiber) exposed to elevated temperatures from 20 °C to 500 °C. The presence of brucite (B, $Mg(OH)_2$), dypingite (D, $Mg_5(CO_3)_4(OH)_2{\cdot}5H_2O$), nesquehonite (N, $MgCO_3{\cdot}3H_2O$), mullite (Mu, $3Al_2O_3{\cdot}2SiO_2$), hydromagnesite (H, $Mg_5(CO_3)_4(OH)_2{\cdot}4H_2O$) and MgO (M) are confirmed with the characteristic XRD peak irrespective of exposure temperature.

The major peak of MgO (#ICCD 00-045-0946) was detected at $2\theta \approx 43°$, identified as the unreacted MgO. The brucite (#ICCD 00-001-1169) was identified around $2\theta \approx 18.6°$ and 38.3°, which are consistent with the observations reported in Ref. [28]. The observation of residual MgO and brucite at 20 °C indicated the incomplete carbonation during the accelerated carbonation process of MgO-based ECC, which is consistent with the finding in Ref. [10]. The mullite (#ICCD 00-001-0613) existed in the matrix as its peaks were detected at 26.8°. Mullite originates from the raw materials of fly ash and was consistent with the observations

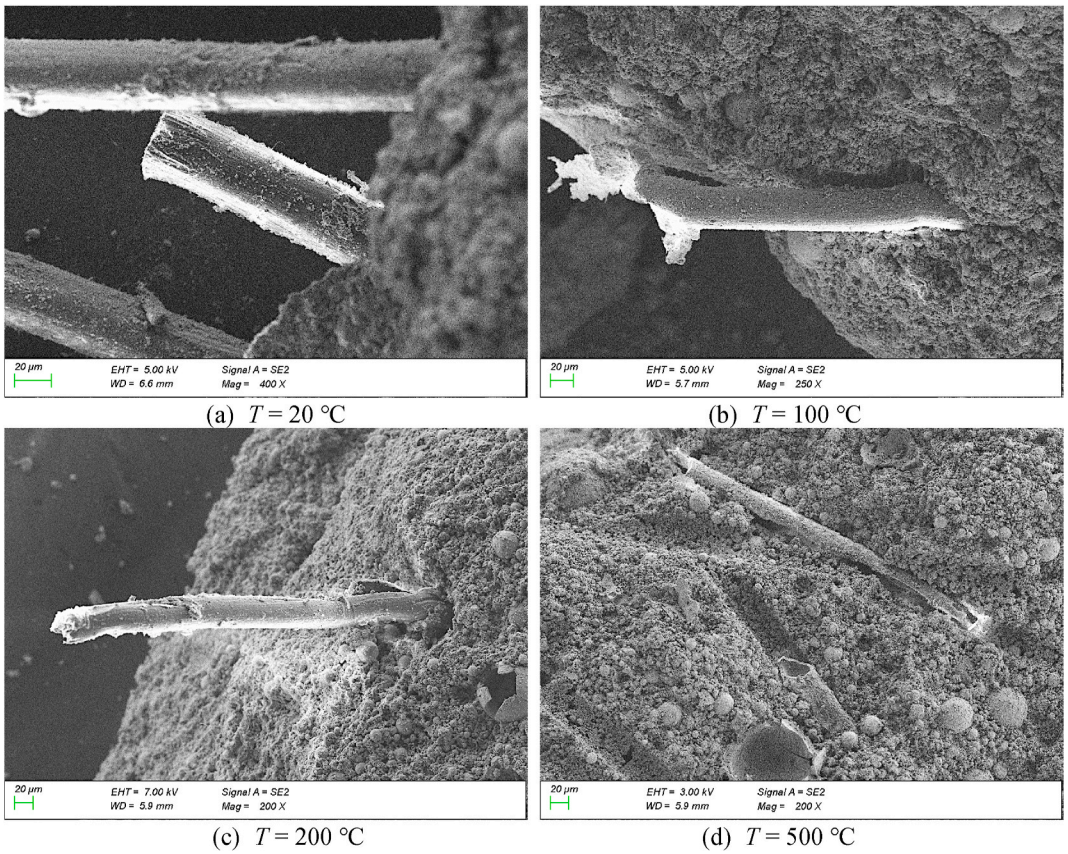

Fig. 11. SEM magnification of carbonated MgO-based ECC under various exposure temperatures.

reported in Ref. [53]. The characteristic peak of dypingite (#ICCD 00-023-1218) was identified at ~20.6° and 30.4°, which is consistent with a previous study [10]. The nesquehonite (#ICCD 00-020-0669) was detected at ~34.2°. The overlapping peak around ~30.4° was detected as the hydromagnesite (#ICCD 00-003-0093) and dypingite (#ICCD 00-023-1218). The data also showed that the reduction of hydromagnesite/dypingite was visible during the process of increasing temperatures. This finding proves that the transformation of hydrated magnesium carbonates during the heating process results in a drop in compressive strength (Fig. 5) and mass loss (Fig. 4).

3.4. Uniaxial tensile performance

Fig. 9 shows the uniaxial tensile stress-strain relationships of the carbonated MgO-based ECC after exposure to different temperatures from 20 °C to 500 °C. The tensile stress-strain curves of specimens exposed to temperatures up to 200 °C show the typical characteristics of ECC: including an initial elastic stage, a strain-hardening stage with the tensile strain capacity over 5%, and a tension-softening stage. In contrast, the tensile stress-strain curve exhibit brittle failure for specimens exposed to 500 °C, which is attributed to the decomposition of PVA fibers.

The change in mechanical properties as a function of exposure temperatures is summarized in Table 3, where "first cracking strength" refers to the tensile stress when the first crack appears. The "tensile strain capacity" and "ultimate tensile strength" are the strain capacity and the maximum tensile stress at specimen failure [10], respectively.

For the carbonated MgO-based ECC at 20 °C, the first cracking strength, ultimate tensile strength, and tensile strain capacity achieved 2.01 MPa, 3.68 MPa, and 5.13%, respectively. The first cracking strength was slightly affected by the elevated temperature below ~200 °C. The highest first cracking strength was found to be 2.11 MPa at 100 °C, which was 8.2% higher than that at 200 °C. Exposure to 50 °C and 100 °C demonstrated that the tensile strain capacity increased with temperature, but the ultimate tensile strength was unaltered. The highest ultimate tensile strength was 3.96 MPa at 200 °C, and the highest tensile strain capacity was 7.91% at 100 °C. These observations indicate that the carbonated MgO-based ECC can maintain the composite properties in terms of tensile strain capacity and tensile strength at temperatures up to 200 °C. However, the first cracking strength, ultimate tensile strength, and tensile strain capacity of carbonated MgO-based ECC were reduced to nearly 0 at 500 °C, which is attributed to the melting of PVA fibers and decomposition of the hydrated magnesium carbonates.

3.5. Multiple crack pattern and fracture surface observation

The tensile crack patterns, including the crack number and crack width within the gauge length of 80 mm are shown in Fig. 10. They confirm the maintenance of tensile ductility through multiple cracking for specimens exposed to elevated temperatures up to 200 °C. At 500 °C, the specimen showed brittle fracture failure. The residual crack widths after unloading, number of cracks, and averaged crack width are given in Table 4. Compared to the specimens at 20 °C, exposure to evaluated temperatures up to 200 °C increased both the crack number and the average crack width.

The fracture surfaces at the final failure of carbonated MgO-based ECC were examined using SEM to identify the failure mechanisms (Fig. 11). For specimens at 20 °C, entire pull-out segments of PVA fiber were observed (Fig. 11 (a)). At elevated temperatures of 100 °C and 200 °C (Fig. 11 (b) and **Fig. 11 (c)**), protruding fibers were observed to have sharpened ends, suggesting fiber rupture following a short pullout stage, likely due to the strengthening of the fiber-matrix interfacial bond accompanied by a decrease in the tensile strength of PVA fibers [54].

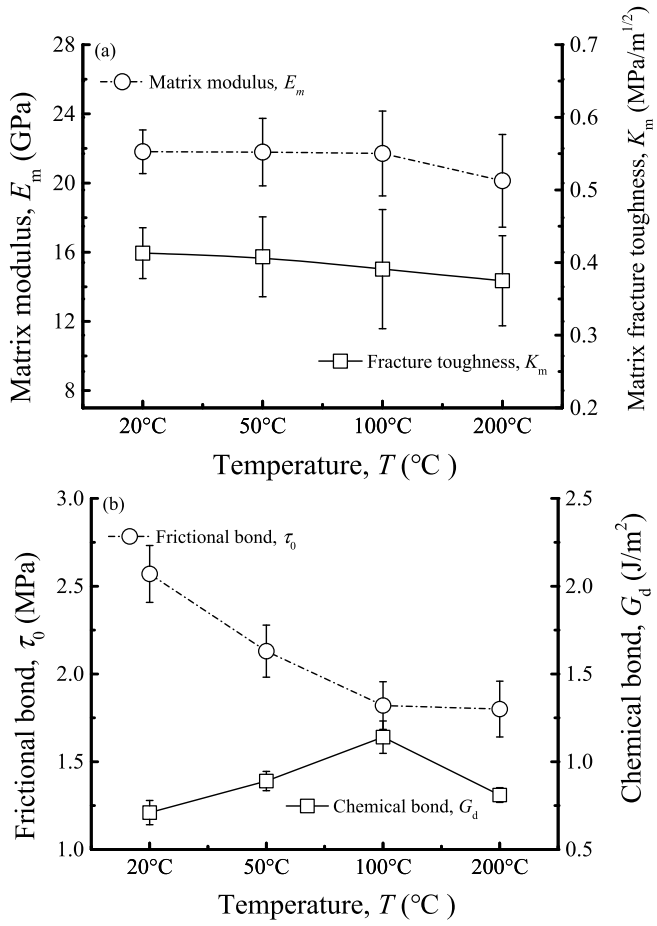

Fig. 12. Variations of (a) Young's modulus and matrix fracture toughness and (b) fiber/matrix interfacial properties under various exposure temperatures.

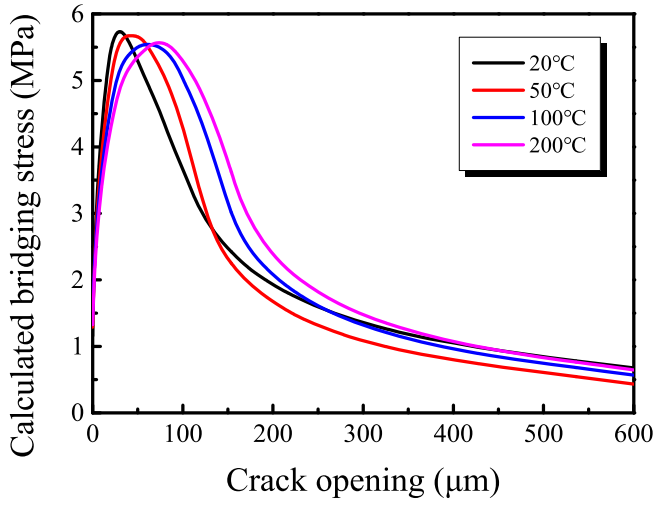

Fig. 13. Computed $\sigma(\delta)$ curve of ECC at various exposure temperatures.

This could explain the lower crack numbers and total residual crack width when the exposure temperature was elevated from 100 °C to 200 °C (Table 4). A few remaining fibers could be seen in specimens exposed to 500 °C (Fig. 11 (d)), suggesting that the temperature of the specimen core had not reached the melting point.

Table 5
Fiber bridging and first crack strength parameters of carbonated MgO-based ECC.

Temperature	σ_0 (MPa)	σ_{fc} (MPa)	σ_0/σ_{fc}	J_{tip} (J/m^2)	J_b' (J/m^2)	J_b'/J_{tip}
20 °C	5.75	2.01	2.87	7.82	33.88	4.33
50 °C	5.67	2.03	2.81	7.64	43.18	5.65
100 °C	5.54	2.11	2.63	7.04	51.76	7.35
200 °C	5.59	1.95	2.87	8.39	54.18	6.46

3.6. Micromechanical analysis

The results of micromechanical parameters, including matrix Young's modulus E_m, fracture toughness K_m, interfacial chemical bond G_d and frictional bond τ_0 are shown in Fig. 12 (a) and (b). E_m and K_m (Fig. 12 (a)) decrease with exposure temperature owing to the damage of the matrix material as noted earlier. The frictional bond τ_0 also shows a decreasing trend. In contrast, the interfacial chemical bond G_d shows an initial rise that may be caused by the higher van der Waals force with the release of free water from the fiber/matrix interface transition zone (ITZ). This increase in G_d may be counteracted by the appearance of microcracks around the ITZ caused by internal vapor pressure as the temperature rises further (for example, up to ~200 °C).

The maximum bridging stress σ_0 and complementary energy J_b' represent important fiber bridging properties that dictate the tensile ductility of ECC [2]. These parameters can be computed from the fiber bridging stress versus crack opening displacement relation (Fig. 13) derived from the fiber/matrix interface properties [2], and are summarized in Table 5. After exposure to elevated temperatures ranged from 50 to 200 °C, J_b'/J_{tip} and σ_0/σ_{fc} which measures the margin of meeting the energy and strength criteria for multiple cracking [2], retain over unity (>2 and 4 respectively), consistent with the observed retaining of tensile ductility of the carbonated MgO-ECC.

4. Conclusions

This study investigated the mechanical and microstructural properties of carbonated MgO-based ECC subjected to elevated temperatures up to 500 °C. Based on the experimental findings, the following conclusions can be drawn:

1) The compressive strength and tensile ductility of carbonated MgO-based ECC are mostly retained under elevated temperature exposures up to 200 °C. However, a significant drop in compressive strength (by 25%) and a complete loss of tensile ductility are found after exposure to 500 °C. Despite this, carbonated MgO-ECC maintains a compressive strength 67% higher than that of mortar without fiber after exposure to 500 °C.
2) Physically, degradation from elevated temperatures resulted in mass loss of PVA fiber due to fiber decomposition, and mass loss in matrix material due to water evaporation and dehydration of magnesium carbonates. Consistent with the observation of macroscopic physical mechanical properties deterioration, these mass losses become significant when the exposure temperature exceeds 200 °C.
3) Despite a general loss in matrix stiffness, fracture toughness and fiber/matrix interface frictional bond with increasing exposure temperatures, the energy-based strain-hardening index J_b'/J_{tip} of carbonated MgO-ECC remarkably increased (30–70%) above that of the composite with no elevated temperature exposure. This provides a micromechanics-based explanation for the composite ductility and multiple cracking maintenance observed, at least up to 200 °C. Above this temperature, however, the carbonated MgO-based ECC becomes brittle as the melting of the PVA fibers disrupts any remaining fiber bridging effect.

4) Microstructurally, an increase in pore size and cumulative pore volume was observed which can be attributed to the decomposition of carbonated MgO-based matrix and PVA fiber at elevated temperatures. The dehydroxylation and decomposition reactions led to a transformation of hydrated magnesium carbonates in the carbonated MgO-based ECC.

The above findings should form a useful basis for further studies of carbonated MgO-based ECC for fire resistance design of civil infrastructures. This study reveals a relatively slow degradation at the composite and microstructural level at exposure temperature at or below 200 °C, but becomes significant at exposure temperature at 500 °C. Future studies should delineate this degradation acceleration by testing at temperature between 200 and 500 °C. Finally, given the melting of PVA fibers at temperature above 200 °C, future studies may investigate the mechanical performance of MgO-based ECC reinforced with higher temperature resistant fibers, such as carbon, basalt, steel fibers or their hybrids.

Declaration of competing interest

The authors declare that they have no known competing financial interests or personal relationships that could have appeared to influence the work reported in this paper.

Acknowledgments

The authors greatly appreciated financial support from the US Department of Energy (DE-FE0030684) and the University of Michigan College of Engineering Blue Sky Research Program. The first author acknowledges the support by a grant from the Chinese Scholarship Council, which enables his study at the Advanced Civil Engineering Materials Research Laboratory (ACE-MRL) at the University of Michigan.

References

[1] V.C. Li, D.K. Mishra, A.E. Naaman, J.K. Wight, J.M. LaFave, H.-C. Wu, Y. Inada, On the shear behavior of engineered cementitious composites, Adv. Cement Base Mater. 3 (1994) 142–149, https://doi.org/10.1016/1065-7355(94)90045-0.
[2] V.C. Li, Engineered Cementitious Composites (ECC), Springer Berlin Heidelberg, 2019, https://doi.org/10.1007/978-3-662-58438-5_1.
[3] V.C. Li, On engineered cementitious composites (ECC), J. Adv. Concr. Technol. 1 (3) (2003) 215–230, https://doi.org/10.3151/jact.1.215.
[4] H.L. Wu, D. Zhang, Y.J. Du, V.C. Li, Durability of engineered cementitious composite exposed to acid mine drainage, Cement Concr. Compos. 108 (2020) 103550, https://doi.org/10.1016/j.cemconcomp.2020.103550.
[5] D. Zhang, H. Wu, V.C. Li, B.R. Ellis, Autogenous healing of Engineered Cementitious Composites (ECC) based on MgO-fly ash binary system activated by carbonation curing, Construct. Build. Mater. (2020) 117672, https://doi.org/10.1016/j.conbuildmat.2019.117672.
[6] D. Zhang, J. Yu, H. Wu, B. Jaworska, B.R. Ellis, V.C. Li, Discontinuous micro-fibers as intrinsic reinforcement for ductile Engineered Cementitious Composites (ECC), Compos. B Eng. 184 (2020) 107741, https://doi.org/10.1016/j.compositesb.2020.107741.
[7] H.L. Wu, J. Yu, D. Zhang, J.-X. Zheng, V.C. Li, Effect of morphological parameters of natural sand on mechanical properties of engineered cementitious composites, Cement Concr. Compos. 100 (2019) 108–119, https://doi.org/10.1016/j.cemconcomp.2019.04.007.
[8] B.T. Huang, J.Q. Wu, J. Yu, J.G Dai, C.K.Y. Leung, V.C. Li, Seawater sea-sand engineered/strain-hardening cementitious composites (ECC/SHCC): Assessment and modeling of crack characteristics, Cement Concr. Res. (2021), https://doi.org/10.1016/j.cemconres.2020.106292.
[9] R.M. Andrew, Global CO_2 emissions from cement production, Earth Syst. Sci. Data 10 (1) (2018) 195.
[10] H.L. Wu, D. Zhang, B.R. Ellis, V.C. Li, Development of reactive MgO-based Engineered Cementitious Composite (ECC) through accelerated carbonation curing, Construct. Build. Mater. 191 (2018) 23–31, https://doi.org/10.1016/j.conbuildmat.2018.09.196.
[11] J. Yu, C. Lu, C.K.Y. Leung, G. Li, Mechanical properties of green structural concrete with ultrahigh-volume fly ash, Construct. Build. Mater. 147 (2017) 510–518, https://doi.org/10.1016/j.conbuildmat.2017.04.188.
[12] J. Yu, H.L. Wu, C.K.Y. Leung, Feasibility of using ultrahigh-volume limestone-calcined clay blend to develop sustainable medium-strength Engineered Cementitious Composites (ECC), J. Clean. Prod. 262 (2020) 121343, https://doi.org/10.1016/j.jclepro.2020.121343.
[13] R. Hay, K. Celik, Hydration, carbonation, strength development and corrosion resistance of reactive MgO cement-based composites, Cement Concr. Res. 128 (2020) 105941, https://doi.org/10.1016/j.cemconres.2019.105941.
[14] S. Ruan, C. Unluer, Influence of mix design on the carbonation, mechanical properties and microstructure of reactive MgO cement-based concrete, Cement Concr. Compos. 80 (2017) 104–114, https://doi.org/10.1016/j.cemconcomp.2017.03.004.
[15] S.A. Walling, J.L. Provis, Magnesia-based cements: a journey of 150 years, and cements for the future, Chem. Rev. 116 (7) (2016) 4170–4204, https://doi.org/10.1021/acs.chemrev.5b00463.
[16] C. Unluer, A. Al-Tabbaa, Impact of hydrated magnesium carbonate additives on the carbonation of reactive MgO cements, Cement Concr. Res. 54 (2013) 87–97, https://doi.org/10.1016/j.cemconres.2013.08.009.
[17] M. Liska, L.J. Vandeperre, A. Al-Tabbaa, Influence of carbonation on the properties of reactive magnesia cement-based pressed masonry units, Adv. Cement Res. 20 (2) (2008) 53–64, https://doi.org/10.1680/adcr.2008.20.2.53.
[18] L. Mo, D.K. Panesar, Accelerated carbonation–A potential approach to sequester CO_2 in cement paste containing slag and reactive MgO, Cement Concr. Compos. 43 (2013) 69–77, https://doi.org/10.1016/j.cemconcomp.2013.07.001.
[19] N.T. Dung, C. Unluer, Improving the performance of reactive MgO cement-based concrete mixes, Construct. Build. Mater. 126 (2016) 747–758, https://doi.org/10.1016/j.conbuildmat.2016.09.090.
[20] R. Zhang, N. Bassim, D.K. Panesar, Characterization of Mg components in reactive MgO–Portland cement blends during hydration and carbonation, Journal of CO_2 Utilization 27 (2018) 518–527, https://doi.org/10.1016/j.jcou.2018.08.025.
[21] J. Qiu, S. Ruan, C. Unluer, E.H. Yang, Autogenous healing of fiber-reinforced reactive magnesia-based tensile strain-hardening composites, Cement Concr. Res. 115 (2019) 401–413, https://doi.org/10.1016/j.cemconres.2018.09.016.
[22] S. Ruan, J. Qiu, E.H. Yang, C. Unluer. Influence of crack width on the stiffness recovery and self-healing of reactive magnesia-based binders under CO_2-H2O conditioning. Construct. Build. Mater. 269 (2021): 121360. doi: 10.1016/j.conbuildmat.2020.121360.
[23] S. Ruan, J. Qiu, E.H. Yang, C. Unluer, Fiber-reinforced reactive magnesia-based tensile strain-hardening composites, Cement Concr. Compos. 89 (2018) 52–61, https://doi.org/10.1016/j.cemconcomp.2018.03.002.
[24] Q. Zhang, V.C. Li, Adhesive bonding of fire-resistive engineered cementitious composites (ECC) to steel, Construct. Build. Mater. 64 (2014) 431–439, https://doi.org/10.1016/j.conbuildmat.2014.04.059.
[25] P.S. Bhat, V. Chang, M. Li, Effect of elevated temperature on strain-hardening engineered cementitious composites, Construct. Build. Mater. 69 (2014) 370–380, https://doi.org/10.1016/j.conbuildmat.2014.07.052.
[26] Iso 19706, Guidelines for assessing the fire threat to people, 2011, https://doi.org/10.3403/30150939u.
[27] J. Yu, J. Lin, Z. Zhang, V.C. Li, Mechanical performance of ECC with high-volume fly ash after sub-elevated temperatures, Construct. Build. Mater. 99 (2015) 82–89, https://doi.org/10.1016/j.conbuildmat.2015.09.002.
[28] L. Pu, C. Unluer, Performance and microstructure of carbonated MgO samples under high temperatures, J. Mater. Civ. Eng. 31 (3) (2019), 04019003, https://doi.org/10.1061/(asce)mt.1943-5533.0002624.
[29] P. Ballirano, C. De Vito, S. Mignardi, V. Ferrini, Phase transitions in the MgCO2H2O system and the thermal decomposition of dypingite, $Mg_5(CO_3)_4(OH)_2{\cdot}5H_2O$: Implications for geosequestration of carbon dioxide, Chem. Geol. 340 (2013) 59–67, https://doi.org/10.1016/j.chemgeo.2012.12.005.
[30] S. Teir, S. Eloneva, C.J. Fogelholm, R. Zevenhoven, Fixation of carbon dioxide by producing hydromagnesite from serpentinite, Appl. Energy 86 (2) (2009) 214–218, https://doi.org/10.1016/j.apenergy.2008.03.013.
[31] Y. Xiong, A.S. Lord, Experimental investigations of the reaction path in the MgO–CO_2–H_2O system in solutions with various ionic strengths, and their applications to nuclear waste isolation, Appl. Geochem. 23 (6) (2008) 1634–1659, https://doi.org/10.1016/j.apgeochem.2007.12.035.
[32] X. Luo, W. Sun, S.Y.N. Chan, Effect of heating and cooling regimes on residual strength and microstructure of normal strength and high-performance concrete, Cement Concr. Res. 30 (3) (2000) 379–383, https://doi.org/10.1016/s0008-8846(99)00264-1.
[33] P. Kalifa, F.D. Menneteau, D. Quenard, Spalling and pore pressure in HPC at high temperatures, Cement Concr. Res. 30 (12) (2000) 1915–1927, https://doi.org/10.1016/s0008-8846(00)00384-7.
[34] A. Botha, C.A. Strydom, Preparation of a magnesium hydroxy carbonate from magnesium hydroxide, Hydrometallurgy 62 (3) (2001) 175–183, https://doi.org/10.1016/s0304-386x(01)00197-9.
[35] L. Hopkinson, P. Kristova, K. Rutt, G. Cressey, Phase transitions in the system MgO–CO_2–H_2O during CO_2 degassing of Mg-bearing solutions, Geochem. Cosmochim. Acta 76 (2012) 1–13, https://doi.org/10.1016/j.gca.2011.10.023.
[36] M. Şahmaran, E. Özbay, H.E. Yücel, M. Lachemi, V.C. Li, Effect of fly ash and PVA fiber on microstructural damage and residual properties of engineered cementitious composites exposed to high temperatures, J. Mater. Civ. Eng. 23 (12) (2011) 1735–1745, https://doi.org/10.1061/(asce)mt.1943-5533.0000335.
[37] C. Wu, V.C. Li, Thermal-mechanical behaviors of CFRP-ECC hybrid under elevated temperatures, Compos. B Eng. 110 (2017) 255–266, https://doi.org/10.1016/j.compositesb.2016.11.037.
[38] P.S. Bhat, V. Chang, M. Li, Effect of elevated temperature on strain-hardening engineered cementitious composites, Construct. Build. Mater. 69 (2014) 370–380, https://doi.org/10.1016/j.conbuildmat.2014.07.052.

[39] K.Q. Yu, J.G. Dai, Z.D. Lu, C.K. Leung, Mechanical properties of engineered cementitious composites subjected to elevated temperatures, J. Mater. Civ. Eng. 27 (10) (2015), 04014268, https://doi.org/10.1061/(asce)mt.1943-5533.0001241.
[40] V. Mechtcherine, F. de Andrade Silva, S. Müller, P. Jun, T.R.D. oledo Filho, Coupled strain rate and temperature effects on the tensile behavior of strain-hardening cement-based composites (SHCC) with PVA fibers, Cement Concr. Res. 42 (11) (2012) 1417–1427, https://doi.org/10.1016/j.cemconres.2012.08.011.
[41] Y. Li, E.H. Yang, K.H. Tan, Effects of heating followed by water quenching on strength and microstructure of ultra-high performance concrete, Construct. Build. Mater. 207 (2019) 403–411, https://doi.org/10.1016/j.conbuildmat.2019.02.123.
[42] Astm C151, Standard Test Method for Autoclave Expansion of Hydraulic Cement, ASTM International, West Conshohocken, PA, 2018.
[43] Astm C618, Standard Specification for Coal Fly Ash and Raw or Calcined Natural Pozzolan for Use in Concrete, ASTM International, West Conshohocken, PA, 2019.
[44] H. Tan, J. Huang, B. Ma, X. Li, Effect of superplasticiser and sodium tripolyphosphate on fluidity of cement paste, Mag. Concr. Res. 66 (2014) 1194–1200, https://doi.org/10.1680/macr.14.00091.
[45] D. Fan, H. Ding, D.Y. Wang, D. Jiang, Field test of optical and electrical fire detectors in simulated fire scenes in a cable tunnel, Photonic Sensors 4 (2) (2014) 156–161, https://doi.org/10.1007/s13320-014-0174-3.
[46] M. Sahmaran, M. Lachemi, V.C. Li, Assessing mechanical properties and microstructure of fire-damaged engineered cementitious composites, ACI Mater. J. 107 (3) (2010), https://doi.org/10.14359/51663759.
[47] Astm C109, Standard Specification for Compressive Strength of Hydraulic Cement Mortars, ASTM International, West Conshohocken, PA, 2013.
[48] Jsce, Recommendations for Design and Construction of High Performance Fiber Reinforced Cement Composites with Multiple Fine Cracks (HPFRCC). Concrete Committee, Rokugo K. (Chair), Japan Society of Civil Engineers, March, 2008, p. 212.
[49] Astm E 399, Standard Test Method for Linear-Elastic Plane-Strain Fracture Toughness of Metallic Materials, ASTM International, West Conshohocken, PA, 2020.
[50] Comite Euro-International du Benton (Ceb), CEB-FIP Model Code 90, 203, Bulletin d'information., Paris, 1990.
[51] R. Hay, K. Celik, Accelerated carbonation of reactive magnesium oxide cement (RMC)-based composite with supercritical carbon dioxide (scCO2), J. Clean. Prod. 248 (2020) 119282, https://doi.org/10.1016/j.jclepro.2019.119282.
[52] J.H. Canterford, G. Tsambourakis, B. Lambert, Some observations on the properties of dypingite, $Mg_5(CO_3)_4(OH)_2{\cdot}5H_2O$, and related minerals, Mineral. Mag. 48 (34) (1984) 437–442, https://doi.org/10.1180/minmag.1984.048.348.15.
[53] S. Gomes, M. François, Characterization of mullite in silicoaluminous fly ash by XRD, TEM, and 29Si MAS NMR, Cement Concr. Res. 30 (2) (2000) 175–181, https://doi.org/10.1016/s0008-8846(99)00226-4.
[54] M.A. Kewalramani, O.A. Mohamed, Z.I. Syed, Engineered cementitious composites for modern civil engineering structures in hot arid coastal climatic conditions, Procedia Engineering 180 (2017) 767–774, https://doi.org/10.1016/j.proeng.2017.04.237.